

INVESTIGATION OF FLOW STRUCTURE INSIDE SPOOL VALVE WITH FEM AND PIV METHODS

Dianrong Gao

College of Mechanical Engineering, Yanshan University, Qinhuangdao, Hebei Province, 066004, P. R. China
gaodr@ysu.edu.cn

Department of Mechanical Engineering, Louisiana State University, Baton Rouge, LA 70803, USA (current)
dgao2@lsu.edu

Abstract

In this paper, the finite element method (FEM) and particle image velocimetry (PIV) techniques are utilized to obtain the flow field along the inlet passage, chamber, metering port, and outlet passage of a spool valve at several different geometrical dimensions. For numerical simulation, the stream function ψ and vorticity ω forms of continuity and Navier-Stokes equations are employed, and the finite element method is applied to discretize the equations. Self-developed simulation codes are executed to compute the values of the stream function and vorticity at each node in the flow domain. Then, according to the correlation between the stream function and velocity components, the velocity vectors of the entire field are calculated. For particle image velocimetry experiments, a pulse Nd: YAG laser is exploited to generate a laser beam. Convex and concave lenses are combined with each other to produce a 1.5-2 mm thickness laser sheet to illuminate the desired plane. Polystyrene spherical particles with a diameter of 30-50 μm are seeded into the fluid as tracing particles. A Kodak ES1.0 CCD camera is employed to capture the images of interest. The images are processed by FFT cross-correlation algorithm, and the processing results are displayed in the form of velocity vector plots. Numerical simulation results and PIV experiments both show that there are three main areas in the spool valve where vortices are formed. Numerical results also indicate that the valve opening and the chamber dimensions have some effects on the flow structure of the valve. The investigation is helpful for qualitatively analyzing the energy loss, noise generation, and steady state flow forces. It can even help in designing the geometrical structure and flow passage.

Keywords: flow field, spool valve, finite element method (FEM), particle image velocimetry (PIV)

1 Introduction

Spool valves are widely used in fluid power transmission and control systems. They are applied as the main stage of directional control valves and even as pressure control valves and servo-valves. The flow structure inside a spool valve has significant effects on the performance of the valve, thus influencing the property of the whole power systems. Therefore, to investigate the flow structure inside the valve, to analyze the energy loss and to study the steady state flow force acting on the spool by numerical calculation and/or experimental methods has become more and more important in recent years. Many scholars and researchers have been attracted to these research aspects, and some fruitful achievements have been reached. Kipping (1996) applied experimental and

numerical methods to investigate the flow in the hydraulic spool valve extensively. Borghi (2000) dealt with the application of a simplified numerical analysis of the flow field inside the compensation port connections of a reference spool valve based on computational fluid dynamics (CFD). Their objective of study was to evaluate the proposed analysis procedure, to verify the effects related to the presence of steady state flow forces affecting the spool equilibrium. Yuan (2002 and 2002) used fundamental momentum and CFD analysis to consider the effect of fluid viscosity on the steady flow force for both positive and negative damping lengths. Their research focused on alleviating the need for large solenoids in the single stage spool valve by advantageously using fluid flow forces. Bao (2001) numerically investigated the flow behavior inside a spool valve, and analyzed the relation between flux, port geometry and pressure loss. Wang (1997) and Ruan (1997) used the PIV method to acquire data in the spool chamber. Vaughan (1992) used the finite

This manuscript was received on 13 May 2003 and was accepted after revision for publication on 12 November 2003

difference method to investigate the spool valve flow field and flow force compensation. The object of present investigation is a two-dimensional spool valve geometry model that is different from the models used in papers mentioned above. The finite element method is applied to discretize the stream function ψ - vorticity ω forms of continuity and Navier-Stokes equations. Self-developed simulation codes are executed to compute the stream function, vorticity, and velocity components in the flow domain. The particle image velocimetry technique is used to validate numerical simulations. It is shown that the main flow structure obtained by FEM simulation is in good agreement with that accomplished by PIV experiments. The main purposes of the paper are to investigate quantitatively the influence of the valve opening and chamber dimensions on the flow structure, such as velocity distribution, flow separation, vortex formation, jet angle, and velocity magnitude at the metering port. Also the energy loss, noise generation and steady state flow forces are investigated qualitatively.

2 Geometry Model, Governing Equations and Discretization with FEM

2.1 Geometry Model

The practical geometrical structure of a spool valve is complex. It is mainly composed of sleeve, spool land, spool rod, metering port, inlet passage, and outlet passage. Taking account of the symmetrical feature of a spool valve, a two-dimensional geometry model is used in this paper. The computational domain includes the chamber and both the inlet and outlet passages, as shown in Fig. 1. The simplifications made in the geometry model of a spool valve are reasonable; the model can really present the main characteristics of the valve.

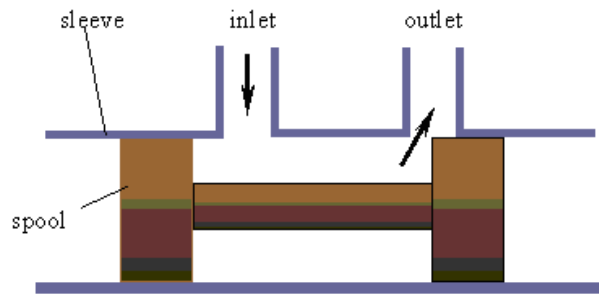


Fig. 1: Simplified geometry model of a spool valve

2.2 Mathematical Model

The flow medium is considered to be an incompressible, viscous Newtonian fluid. Density and viscosity of the fluid are assumed to be temperature independent. The following assumptions are adopted. (1) No slip conditions on all spool land faces, spool rod, and sleeve walls. (2) Constant flux at the inlet port. (3) No clearance between sleeve and spool land.

Introducing the index notations for two-dimensional

incompressible laminar flow, the continuity equation is expressed by

$$\frac{\partial u_i}{\partial x_i} = 0 \quad (i=1, 2) \quad (1)$$

The time-dependent Navier-Stokes equation is described as

$$\frac{\partial u_i}{\partial t} + u_j \frac{\partial u_i}{\partial x_j} = f_i - \frac{\partial P}{\partial x_i} + \nu \frac{\partial^2 u_i}{\partial x_j \partial x_j} \quad (2)$$

where P is the so-called kinematic pressure (pressure divided by density) (Wendt, 1996) and ν is the kinematic viscosity.

In Eq. 1 and 2, repeated indices imply summing, $i=1, 2, j=1, 2$.

The continuity Eq. 1 can be satisfied by the introduction of the stream-function ψ , and velocity components are written as

$$u_i = \varepsilon_{ij} \frac{\partial \psi}{\partial x_j} \quad (i=1, 2, j=1, 2) \quad (3)$$

where ε_{ij} is the permutation symbol defined as by Chung (1978)

$$\varepsilon_{ij} = \begin{cases} 1 & i=1, j=2 \\ -1 & i=2, j=1 \\ 0 & i=j \end{cases} \quad (4)$$

For two-dimensional flow, the vorticity ω is introduced by

$$\omega = \frac{\partial u_2}{\partial x_1} - \frac{\partial u_1}{\partial x_2} = \varepsilon_{ji} \frac{\partial u_i}{\partial x_j} \quad (i=1, 2, j=1, 2) \quad (5)$$

Combining Eq. 3 and 5, the Poisson equation with stream function ψ and vorticity ω is obtained

$$\frac{\partial^2 \psi}{\partial x_j \partial x_j} = -\omega \quad (6)$$

Taking curl to both sides of Eq. 2, and assuming that the body forces f_i have a potential, then

$$\varepsilon_{ij} \frac{\partial f_i}{\partial x_j} = 0 \quad (7)$$

Note that

$$\varepsilon_{ij} \frac{\partial^2 P}{\partial x_i \partial x_j} = \frac{\partial^2 P}{\partial x_1 \partial x_2} - \frac{\partial^2 P}{\partial x_2 \partial x_1} = 0 \quad (8)$$

then

$$\begin{aligned} \frac{\partial}{\partial t} \left(\varepsilon_{ij} \frac{\partial u_i}{\partial x_j} \right) + u_k \frac{\partial}{\partial x_k} \left(\varepsilon_{ij} \frac{\partial u_i}{\partial x_j} \right) \\ = \nu \frac{\partial^2}{\partial x_k \partial x_k} \left(\varepsilon_{ij} \frac{\partial u_i}{\partial x_j} \right) \end{aligned} \quad (9)$$

Substituting Eq. 5 into 9, the momentum equation is transferred into the vorticity transport equation expressed by the stream function ψ and vorticity ω

$$\frac{\partial \omega}{\partial t} + \varepsilon_{ij} \frac{\partial \psi}{\partial x_j} \frac{\partial \omega}{\partial x_i} = \nu \frac{\partial^2 \omega}{\partial x_k \partial x_k} \quad (10)$$

It is often considered convenient to write Eq. 6 and 10 in a non-dimensional form in terms of the Reynolds number

$$\frac{\partial^2 \psi}{\partial x_j \partial x_j} = -\omega \quad (11a)$$

$$\frac{\partial \omega}{\partial t} + \varepsilon_{ij} \frac{\partial \psi}{\partial x_j} \frac{\partial \omega}{\partial x_i} = \frac{1}{\text{Re}} \frac{\partial^2 \omega}{\partial x_k \partial x_k} \quad (11b)$$

where Re is the Reynolds number, $\text{Re} = u_0 L / \nu$ with L the characteristic length, u_0 the free stream velocity, and $x_i = \bar{x}_i / L$ and $t = \bar{t} / (L / u_0)$ and $u_i = \bar{u}_i / u_0$ and $\psi = \bar{\psi} / (u_0 L)$ and $\omega = \bar{\omega} / (u_0 / L)$. The over bars indicate the physical quantities.

2.3 Finite Element Analysis

The finite element method is an approximate method of solving differential equations of boundary and/or initial value problems in engineering and mathematical physics. The procedure employs subdivision of the solution domain into many smaller regions of convenient shapes, such as triangular, quadrilateral, etc. Choosing suitable points called “nodes” within the element, the variables in the differential equations are written as a linear combination of approximately selected interpolation functions and the values of the variable or its various derivatives are specified at the nodes. Using the variational principle or weighted residual methods, the governing differential equations are transformed into “finite element equations” governing all isolated elements. These local elements are finally collected together to form a global system of differential or algebraic equations with proper boundary and/or initial conditions imposed. The nodal values of the variables are then determined from this system of equations (Baker, 1983; Chung, 1975).

The mathematical principle underlying the finite element method is an approximate evaluation of the symmetric Galerkin weak statement constructed from the governing differential equation with boundary conditions (Baker, 1991).

The Galerkin weak formulae of Eq. 11 are

$$\iint_{\Omega} \left(\frac{\partial^2 \psi}{\partial x_j \partial x_j} + \omega \right) \delta \psi \, d\Omega = 0 \quad (12a)$$

$$\iint_{\Omega} \left(\frac{\partial \omega}{\partial t} + \varepsilon_{ij} \frac{\partial \psi}{\partial x_j} \frac{\partial \omega}{\partial x_i} - \frac{1}{\text{Re}} \frac{\partial^2 \omega}{\partial x_k \partial x_k} \right) \delta \omega \, d\Omega = 0 \quad (12b)$$

Assuming that the natural boundary conditions of stream function ψ and vorticity ω are

$$\frac{\partial \psi}{\partial n} = -u_s \quad (\text{on } \Gamma_u) \quad (13a)$$

$$\frac{\partial \omega}{\partial n} = g \quad (\text{on } \Gamma_\omega) \quad (13b)$$

Applying the Green-Gauss theorem and noting the boundary conditions of Eq. 13, the weak formulation of the Galerkin Weighted Residual of Eq. 12 can be denoted as

$$\iint_{\Omega} \left(\frac{\partial \psi}{\partial x_j} \frac{\partial (\delta \psi)}{\partial x_j} - \omega \delta \psi \right) d\Omega = - \int_{\Gamma_u} u_s \delta \psi \, d\Gamma \quad (14a)$$

$$\iint_{\Omega} \left[\left(\frac{\partial \omega}{\partial t} + \varepsilon_{ij} \frac{\partial \psi}{\partial x_j} \frac{\partial \omega}{\partial x_i} \right) \delta \omega + \frac{1}{\text{Re}} \frac{\partial \omega}{\partial x_k} \frac{\partial (\delta \omega)}{\partial x_k} \right] d\Omega = \int_{\Gamma_\omega} \frac{1}{\text{Re}} \delta \omega \, d\Gamma \quad (14b)$$

Assuming local interpolation functions of ψ , ω in the finite element

$$\psi = \psi_i(t) N_i \quad (15)$$

$$\omega = \omega_i(t) M_i \quad (16)$$

where, $\psi_i(t)$, $\omega_i(t)$ are the values of the stream function and vorticity at the i th node in the element at time t . $N_i = N_i(x_j)$, ($j=1, 2$) is the shape function of the stream function ψ . $M_i = M_i(x_j)$, ($j=1, 2$) is the shape function of vorticity ω . In this paper, the shape functions of ψ and ω are identical, that is $N_i = N_i(x_j) = M_i(x_j)$.

Substituting Eq. 15 and 16 into 14, and replacing $\delta \psi$ with a weighted function, that is base function $N_i(x_j)$, the local finite element equations are obtained

$$\mathbf{E}_{ij}^{(e)} \boldsymbol{\psi}_j - \mathbf{F}_{ij}^{(e)} \boldsymbol{\omega}_j = \mathbf{G}_i^{(e)} \quad (17a)$$

$$\mathbf{A}_{ij}^{(e)} \dot{\boldsymbol{\omega}}_j + \mathbf{B}_{ijk}^{(e)} \boldsymbol{\psi}_j \boldsymbol{\omega}_k + \mathbf{C}_{ij}^{(e)} \boldsymbol{\omega}_j = \mathbf{D}_i^{(e)} \quad (17b)$$

where

$$\mathbf{A}_{ij}^{(e)} = \iint_{\Omega^{(e)}} N_i N_j \, d\Omega \quad (18)$$

$$\mathbf{B}_{ijk}^{(e)} = \iint_{\Omega^{(e)}} N_i \left(\frac{\partial N_j}{\partial x_2} \frac{\partial N_k}{\partial x_1} - \frac{\partial N_j}{\partial x_1} \frac{\partial N_k}{\partial x_2} \right) d\Omega \quad (19)$$

$$\mathbf{C}_{ij}^{(e)} = \frac{1}{\text{Re}} \iint_{\Omega^{(e)}} \left(\frac{\partial N_j}{\partial x_1} \frac{\partial N_i}{\partial x_1} + \frac{\partial N_j}{\partial x_2} \frac{\partial N_i}{\partial x_2} \right) d\Omega \quad (20)$$

$$\mathbf{D}_i^{(e)} = \int_{\Gamma_\omega} \frac{1}{\text{Re}} g N_i \, d\Gamma \quad (21)$$

$$\mathbf{E}_{ij}^{(e)} = \iint_{\Omega^{(e)}} \left(\frac{\partial N_j}{\partial x_1} \frac{\partial N_i}{\partial x_1} + \frac{\partial N_j}{\partial x_2} \frac{\partial N_i}{\partial x_2} \right) d\Omega \quad (22)$$

$$\mathbf{F}_{ij}^{(e)} = \iint_{\Omega^{(e)}} N_i N_j \, d\Omega \quad (23)$$

$$\mathbf{G}_i^{(e)} = - \int_{\Gamma_u} u_s N_i \, d\Gamma \quad (24)$$

In this paper, four-node isoparameter quadrilateral elements are used. Taking four vertices as nodes of the element, four interpolation functions are used. In a non-dimensionalized coordinate system for a four-node square element, Lagrange interpolation functions are selected as follows

$$N_1 = \frac{1}{4}(1-\xi)(1-\eta) \quad (25)$$

$$N_2 = \frac{1}{4}(1+\xi)(1-\eta) \quad (26)$$

$$N_3 = \frac{1}{4}(1+\xi)(1+\eta) \quad (27)$$

$$N_4 = \frac{1}{4}(1-\xi)(1+\eta) \quad (28)$$

Transforming the Cartesian coordinate system (x_i) of Eq. 18-24 into a non-dimensionalized natural coordinate system (η, ξ) and noting that

$$d\Omega = |\mathbf{J}| d\xi d\eta \quad (29)$$

where \mathbf{J} is called Jacobian given by

$$|\mathbf{J}| = \begin{vmatrix} \frac{\partial x_1}{\partial \xi} & \frac{\partial x_2}{\partial \xi} \\ \frac{\partial x_1}{\partial \eta} & \frac{\partial x_2}{\partial \eta} \end{vmatrix} \quad (30)$$

Then

$$\mathbf{A}_{ij}^{(e)} = \iint_{\Omega^{(e)}} N_i N_j d\Omega = \int_{-1}^{+1} \int_{-1}^{+1} |\mathbf{J}| N_i N_j d\eta d\xi \quad (31)$$

$$\mathbf{B}_{ijk}^{(e)} = \int_{-1}^{+1} \int_{-1}^{+1} \frac{1}{|\mathbf{J}|} N_j \left(\frac{\partial x_1}{\partial \xi} \frac{\partial x_2}{\partial \eta} - \frac{\partial x_1}{\partial \eta} \frac{\partial x_2}{\partial \xi} \right) \left(\frac{\partial N_i}{\partial \eta} \frac{\partial N_k}{\partial \xi} - \frac{\partial N_j}{\partial \xi} \frac{\partial N_k}{\partial \eta} \right) d\eta d\xi \quad (32)$$

$$\mathbf{C}_{ij}^{(e)} = \frac{1}{\text{Re}} \int_{-1}^{+1} \int_{-1}^{+1} \frac{1}{|\mathbf{J}|} \left\{ \left[\left(\frac{\partial x_1}{\partial \eta} \right)^2 + \left(\frac{\partial x_2}{\partial \eta} \right)^2 \right] \frac{\partial N_i}{\partial \xi} \frac{\partial N_j}{\partial \xi} + \left[\left(\frac{\partial x_1}{\partial \xi} \right)^2 + \left(\frac{\partial x_2}{\partial \xi} \right)^2 \right] \frac{\partial N_i}{\partial \eta} \frac{\partial N_j}{\partial \eta} - \left(\frac{\partial x_1}{\partial \xi} \frac{\partial x_1}{\partial \eta} + \frac{\partial x_2}{\partial \xi} \frac{\partial x_2}{\partial \eta} \right) \left(\frac{\partial N_i}{\partial \xi} \frac{\partial N_j}{\partial \eta} + \frac{\partial N_i}{\partial \eta} \frac{\partial N_j}{\partial \xi} \right) \right\} d\eta d\xi \quad (33)$$

$$\mathbf{E}_{ij}^{(e)} = \text{Re } \mathbf{C}_{ij}^{(e)} \quad (34)$$

$$\mathbf{F}_{ij}^{(e)} = \mathbf{A}_{ij}^{(e)} \quad (35)$$

Noting that on boundaries

$$\frac{\partial \psi}{\partial n} = -u_s = 0 \quad (36)$$

$$\frac{\partial \omega}{\partial n} = g = 0 \quad (37)$$

then

$$\mathbf{D}_i^{(e)} = 0 \quad (38)$$

$$\mathbf{G}_i^{(e)} = 0 \quad (39)$$

Applying four-point Gaussian quadrature integration to Eq. 31-35, the coefficient matrices and vectors of the local finite element are calculated.

By assembling all the local finite element equations, the global finite element equations are achieved

$$\mathbf{E}_{nm} \boldsymbol{\psi}_m - \mathbf{F}_{nm} \boldsymbol{\omega}_m = \mathbf{G}_n \quad (40a)$$

$$\mathbf{A}_{nm} \dot{\boldsymbol{\omega}}_m + \mathbf{B}_{nmp} \boldsymbol{\psi}_m \boldsymbol{\omega}_p + \mathbf{C}_{nm} \boldsymbol{\omega}_m = \mathbf{D}_n \quad (40b)$$

Since the natural boundary conditions of ψ and ω automatically appear in the resulting local finite element equations, by imposing essential boundary conditions of ψ and ω in Eq. 40 and by applying initial values, Eq. 40 can be solved.

2.4 Solving Procedure

The solving procedure of Eq. 40 with FEM method is described below

(i) Mesh division of flow domain. The number of meshes needed in the flow domain is determined by the flow characteristics and computer capabilities. Usually finer meshes are set in the area where physical quantities vary strongly. In this paper, considering the computer capabilities and convenience of comparing the flow structure at different flow conditions, the flow domain is divided into 796 global elements and 895, 894, 893 global nodes, respectively, while valve openings are 0.375cm, 0.75cm, 1.125cm;

(ii) Read in data about the correlation between the global node number and local element node number, coordinate values of global nodes, essential boundary node number of ψ, ω and their values, natural boundary node number of ψ, ω and their values;

(iii) Set zero to all global coefficient matrices and vectors;

(iv) Calculate local element coefficient matrices and vectors using Eq. 31-35;

(v) Transform local element coefficient matrices and vectors into global coefficient matrices and vectors. Usually in the flow domain, one global node is shared by several local elements around it. The nodes in the local element have contributions to the global nodes. Each time after calculating local element coefficient matrices and vectors and adding them to the global nodes, global coefficient matrices and vectors can be obtained finally;

(vi) Set initial values for ω on all nodes, from Eq. 40a and essential boundary of ω , the stream function ψ on all nodes at time t are solved. Then with known ψ at time t , from Eq. 40b, vorticity ω on all nodes at time $t+\Delta t$ is gained. With known ω at time $t+\Delta t$, from Eq. 40a, the stream function at time $t+\Delta t$ is obtained. Repeating this step, the stream function and vorticity on all nodes at each time step are achieved. Note that in Eq. 40b, $\dot{\boldsymbol{\omega}}_m$ is transformed into $(\omega_{t+\Delta t} - \omega_t)/2\Delta t$ by the central difference formula;

(vii) When $(\omega_{t+\Delta t} - \omega_t)/2\Delta t$ is less than 0.04 (Baker, 1975), the statistic steady state is reached, the values of ψ, ω are considered to be steady state solution, and the program stops running;

(viii) Display and output of the results, end.

3 Computational Results

3.1 Geometry Dimensions and Boundary Conditions of Flow Domain

Taking the valve opening $x_v=1.125$ cm as an example, the flow domain is divided into 796 global elements and 893 global nodes. Geometry sizes and boundary conditions of the flow region are illustrated in Fig. 2.

At the inlet port *al*, assuming $u_1=0$ and u_2 is prescribed as a parabolic profile

$$\bar{u}_2 = -0.4444(2.25 - \bar{x}_1^2) \quad (41)$$

Here over bars indicate dimensional quantities. Assuming that the velocity on the centerline of the inlet passage ($\bar{x}_1 = 0$ cm) is 1 cm/s, this value is considered as free stream velocity u_0 , since the flow at the centerline of the channel is almost free of the disturbance by the walls. Taking the inlet width $L=3.0$ cm as the characteristic length, the non-dimensionalized form of Eq. 41 is

$$u_2 = -0.4444(2.25 - 9x_1^2) \quad (42)$$

On the inlet boundary, the stream function is determined by Eq. 3. Since u_2 changes with x_1 only, then

$$\begin{aligned} \psi &= -\int u_2 dx_1 \\ &= \int 0.4444(2.25 - 9x_1^2) dx_1 \\ &= x_1 - 1.3332x_1^3 \end{aligned} \quad (43)$$

The vorticity is determined by Eq. 5.

$$\omega = \frac{\partial u_2}{\partial x_1} - \frac{\partial u_1}{\partial x_2} = 7.8992x_1 \quad (44)$$

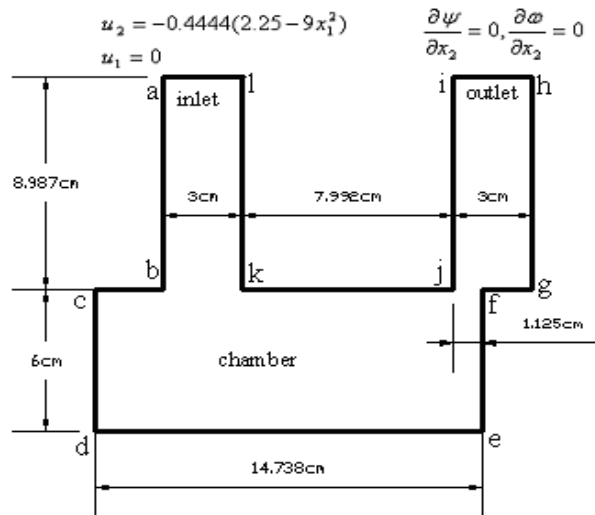


Fig. 2: Geometry dimension and boundary conditions of flow domain

At the outlet boundary *ih*, u_1 can be assumed to be zero and derivatives of the velocity component in the x_2 direction can be assumed to be zero. This means

$$\frac{\partial \psi}{\partial x_2} = 0 \quad \frac{\partial \omega}{\partial x_2} = 0 \quad (45)$$

At solid boundaries *abcdefgh* and *ijkl*, $\psi=\psi_1$ and $\psi=\psi_2$ respectively, and $\frac{\partial \psi}{\partial n} = 0$, here ψ_1 and ψ_2 are determined by Eq. 43, and *n* is the normal direction of the boundaries.

On boundary *abcdefgh* and *ijkl*, the vorticity ω is time dependent, and is determined by solving Eq. 18b at each time step.

3.2 Different Valve Openings

The spool is set in three different positions while keeping the inlet flow rate and pressure constant. The valve openings related to three different spool positions are $x_v=0.375$ cm, 0.75cm, 1.125cm. Considering the computer capacities used and convenience for comparing results of different flow conditions, the flow area is divided into 796 global elements and 895, 894, 893 global nodes, respectively. The characteristic length is $L=3.0$ cm, the free stream velocity is $u_0=1.0$ cm/s, flow medium is water, and its kinematic viscosity is $\nu=1 \times 10^{-2}$ cm²/s. Then Reynolds number $Re = u_0 L / \nu$ is 300. The self-developed simulation programs are executed with time step $\Delta t=0.02$. After about 750 time iterations, $\delta \omega / \delta t$ is less than 0.04, the statistic steady state is reached, and the values of ψ , ω are considered to be steady state solution (Baker, 1975).

The steady state results for three openings are demonstrated in Fig. 3, Fig. 4 and Fig. 5 in the forms of velocity vector plots, stream function contours, and spectral plots, respectively. These figures clearly show that there are three zones inside the valve where vortices are generated. One vortex is formed at the lower left side of the chamber. It is the largest one in size. In Fig. 5 the color of this vortex is changing from green to light yellow to red when the valve opening x_v is changed from 0.375 cm to 0.75 cm to 1.125 cm. The change of color indicates that the vortex intensity is getting stronger and stronger with the increasing valve opening. Thus the energy loss and fluid flow noise caused by this vortex is getting greater and greater when the valve opening increases. Another vortex exists at the upper center of the chamber near the inlet port. The vortex size and color vary a little with the variation of the valve opening in Fig. 4 and Fig. 5. Its intensity is the weakest, and it has little effect on the energy loss and fluid flow noise. The last vortex is located at the upper right corner of the metering port. Its size is getting smaller and smaller with increasing valve opening. Its color is red and varies little with the valve opening. It is the strongest one in intensity. It has a stronger effect on the energy loss and fluid flow noise of the valve than the other two vortices.

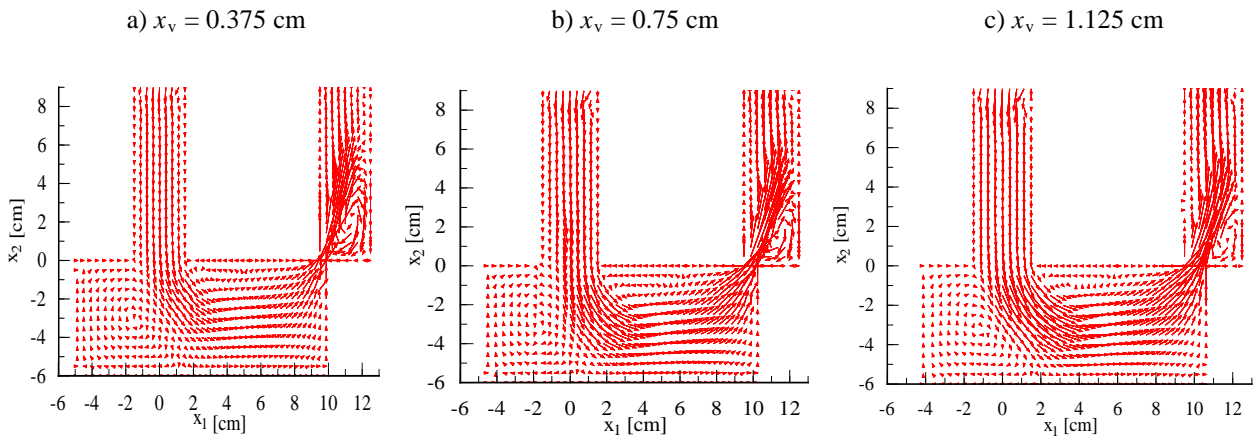


Fig. 3: Velocity vector plots for three different valve openings

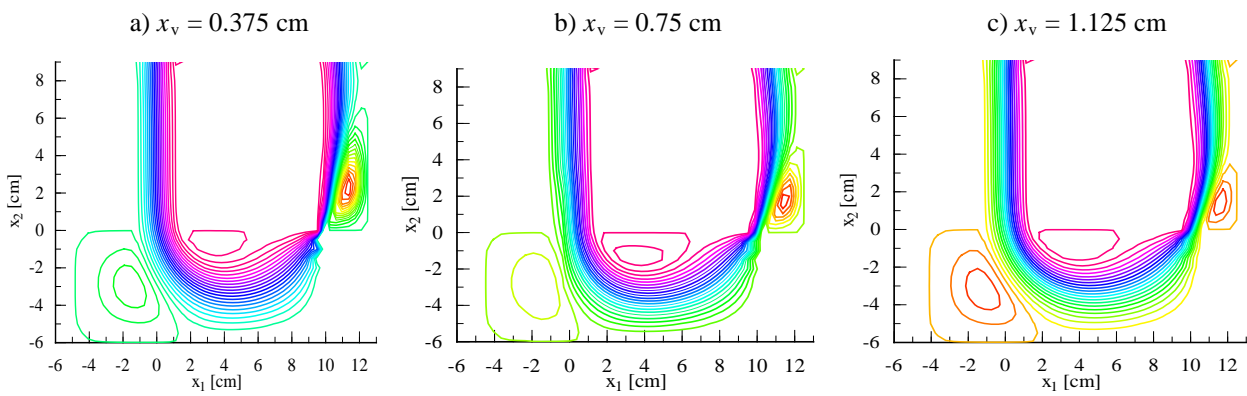


Fig. 4: Stream function contours for three different valve openings

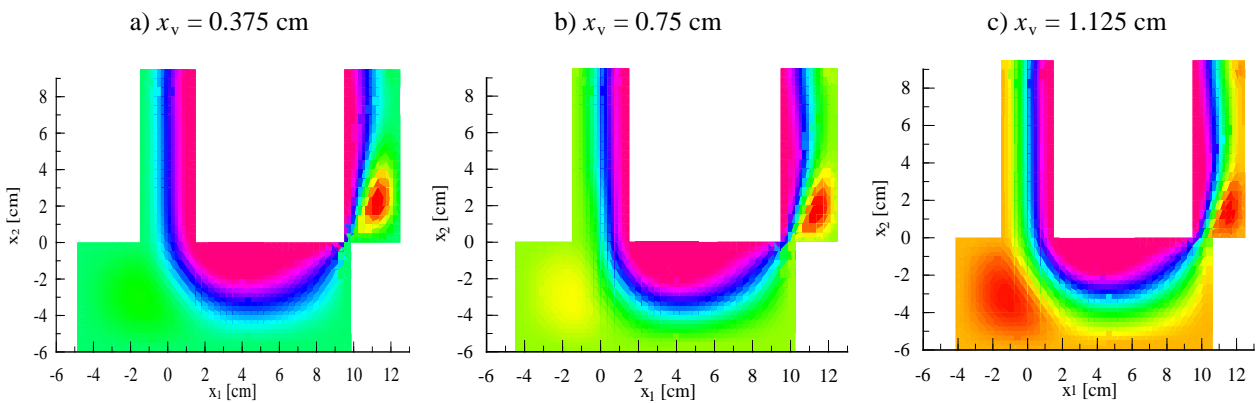


Fig. 5: Spectral plots for three different valve openings

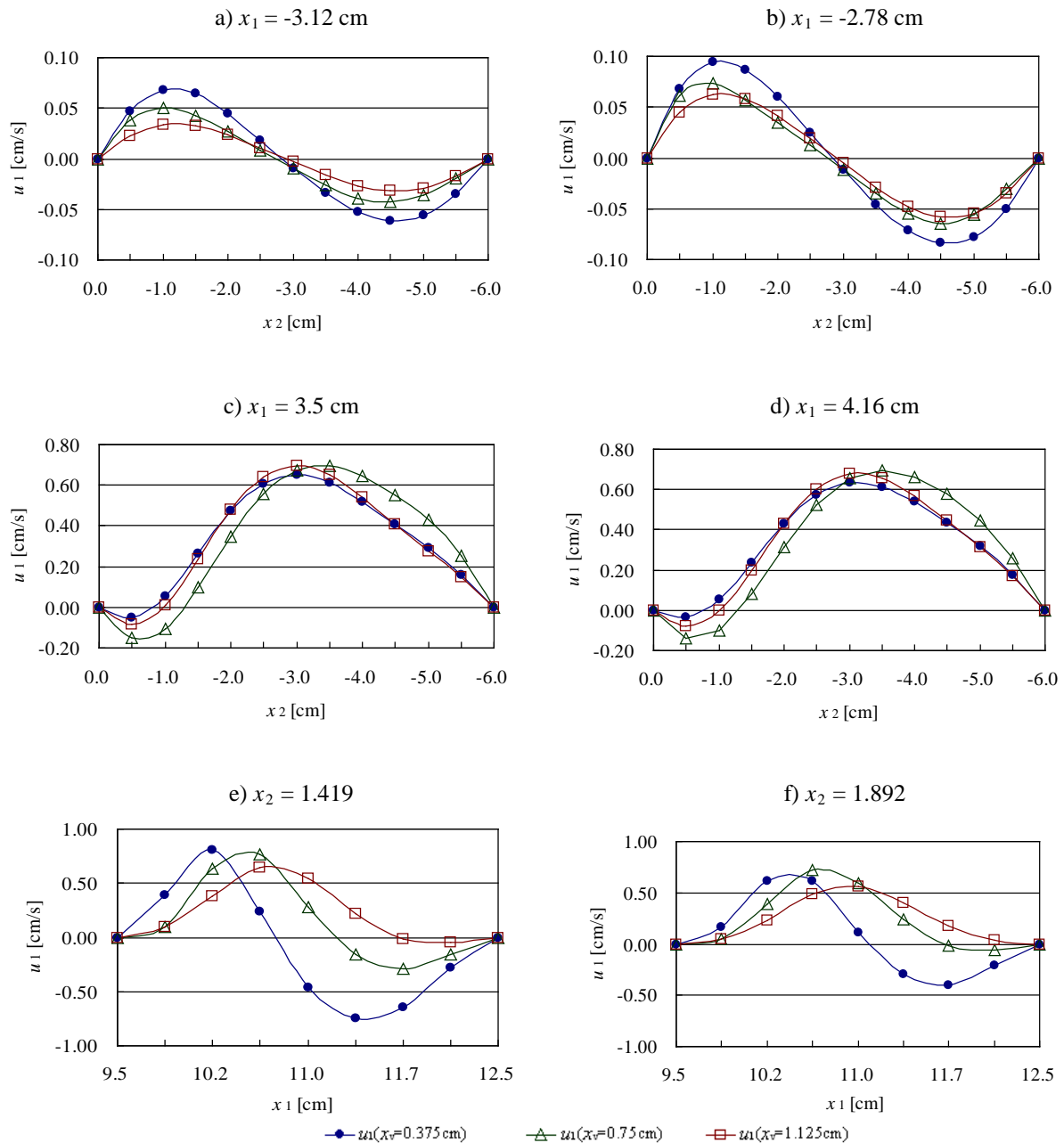


Fig. 6: Horizontal velocity profiles at different positions for three valve opening conditions

Figure 6 shows the horizontal velocities profile for three valve openings at different positions. Fig. 6 a) and b) illustrate the velocity profiles at the lower left region of the valve chamber. The velocity profiles are different for different valve openings. With the increase of valve opening, the value of the velocity along the horizontal axis is decreasing. This results in some difference of the vortices formed at three valve openings. Fig. 6 c) and d) display the velocity profiles near the upper center region of the chamber, the value of velocities varies a little when the valve opening is varied, and the negative velocity is very small. It proves again that the vortex in this region is small and weak, and has little effect on the flow. Fig. 6 e) and f) demonstrate the velocity profile at the region of the upper right corner near the metering port. The value of the velocity is the highest among the three regions

mentioned above, and with the valve opening increasing, the main flow velocity is decreased.

Figure 7 shows the vertical velocity profiles for three valve openings at different positions. Fig. 7 a) and b) illustrate the velocity profiles at the lower left region of the valve chamber. Fig. 7 c) and d) display the velocity profiles near the upper center region of the chamber. In these two regions, when the valve opening is 1.125 cm, the values of velocity are the highest, while for the valve opening 0.75 cm, the values of the velocity are the smallest. For the valve opening of 0.375 cm, the value of the velocity is between that of the valve opening being 1.125 cm and 0.75 cm. Fig. 7 e) and f) demonstrate the velocity profile of the outlet passage near the metering port. The value of the velocity is the highest among the three regions. With the valve opening increasing, the velocity is decreased.

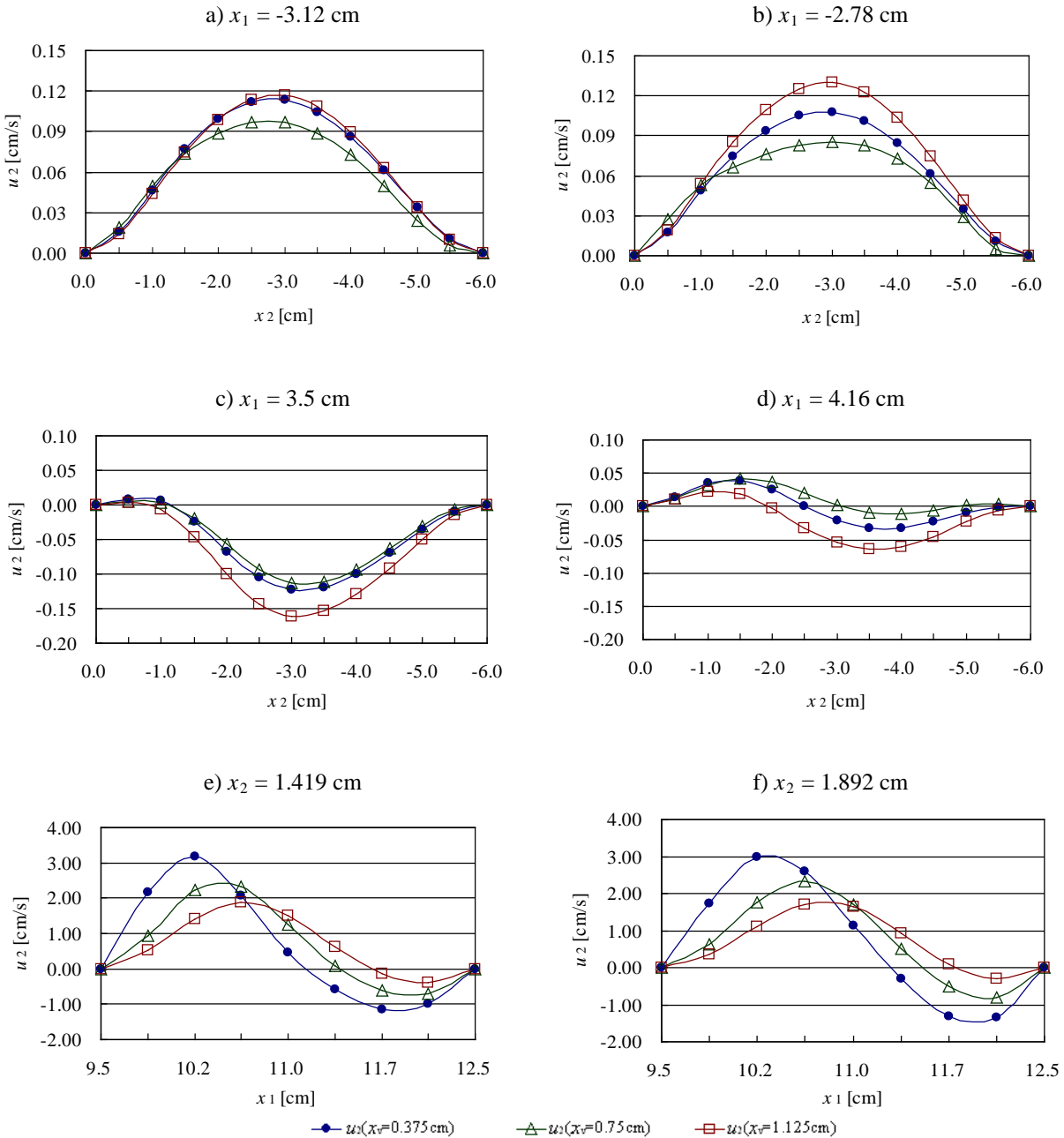


Fig. 7: Vertical velocity profiles at different positions for three valve opening conditions

3.3 Different Chamber Length and Height

When the valve opening is kept at $x_v = 1.125$ cm, the chamber length is changed from originally 7.992 cm to 9.60 cm, and the other conditions are unchanged. The numerical calculation results are presented in Fig. 8 in the forms of velocity vector plot, stream function contours, and spectral plot. A small difference in the flow structure is exhibited only at the left side of the outlet passage near the metering port, where a small vortex is produced. In other parts of the spool valve, the flow structure remains nearly the same as that when the chamber length is 7.992 cm. This viewpoint is further proven by Fig. 9, in which the horizontal and vertical velocity profiles for chamber length 7.992 cm and 9.60

cm are shown at four positions. The velocity profiles are almost the same at the same locations.

Figure 10 shows the numerical results for a chamber height 7.2 cm at the valve opening $x_v=1.125$ cm. In Fig. 11 the velocity profiles for the chamber height 6.0 cm and 7.2 cm are compared at four locations. It is easy to see from these figures that the size of the vortex located at the lower left of the chamber is a little bigger than that of chamber height 6.0 cm, and there is also a small vortex generated at the left side of the outlet passage near the metering port. A little change in flow structure is discovered in other parts of the valve.

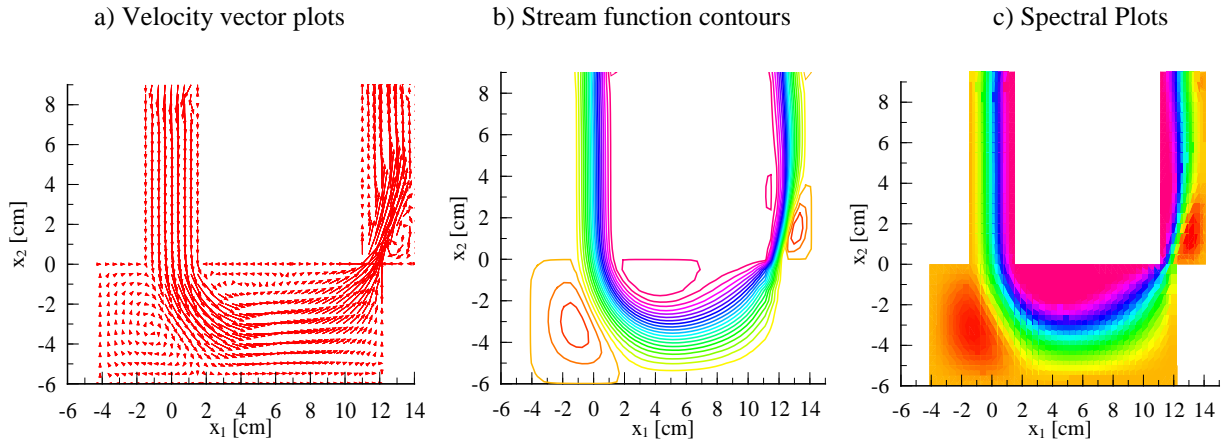


Fig. 8: Calculation results with chamber length 9.60 cm for valve opening 1.125 cm

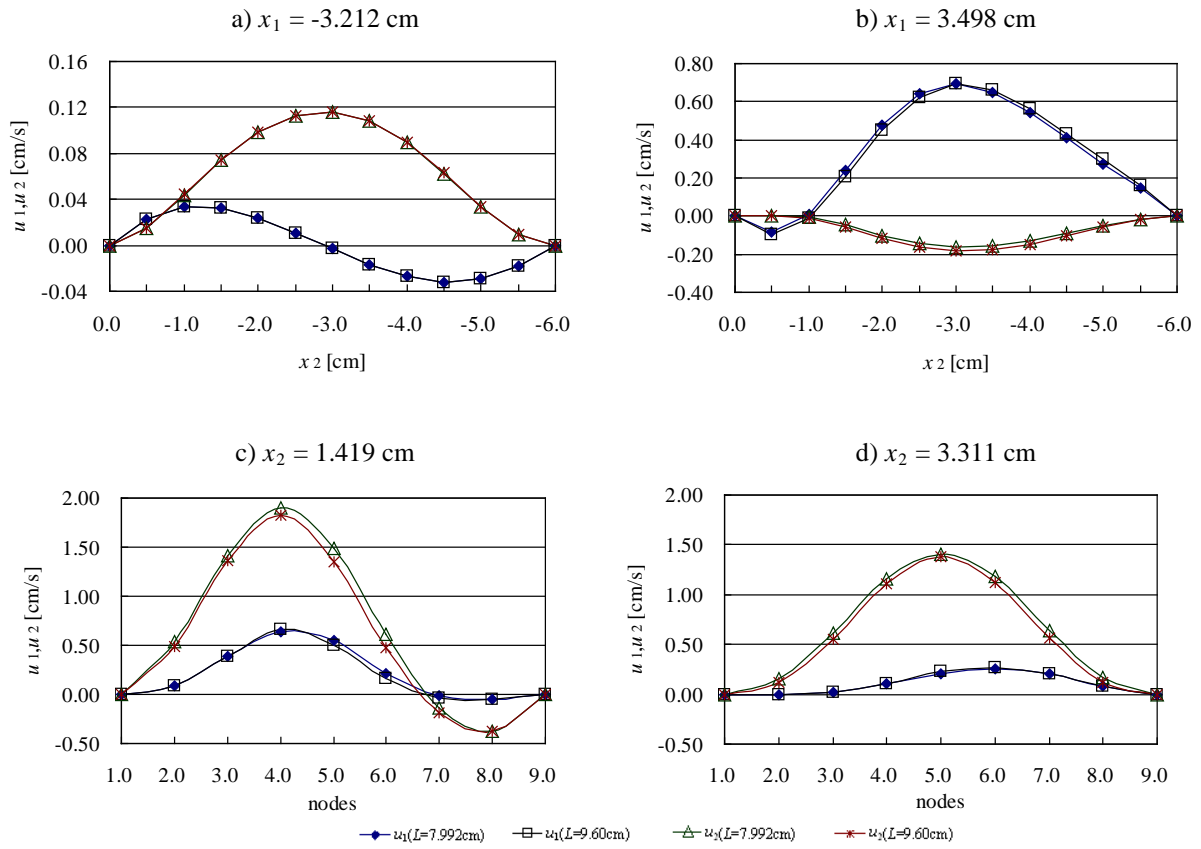


Fig. 9: Velocity profiles with chamber length 7.992 cm and 9.60 cm for valve opening 1.125 cm

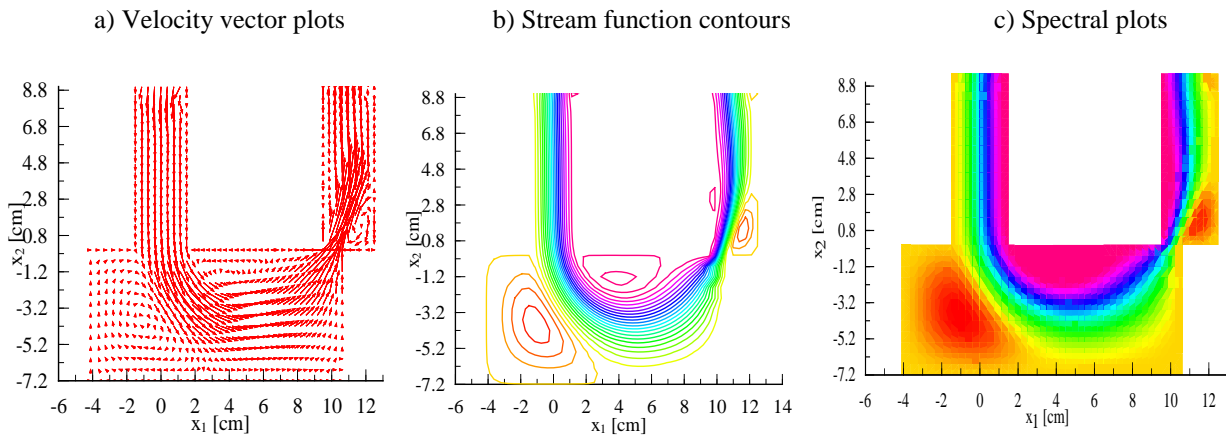


Fig. 10: calculation results with chamber height 7.20 cm for valve opening 1.125 cm

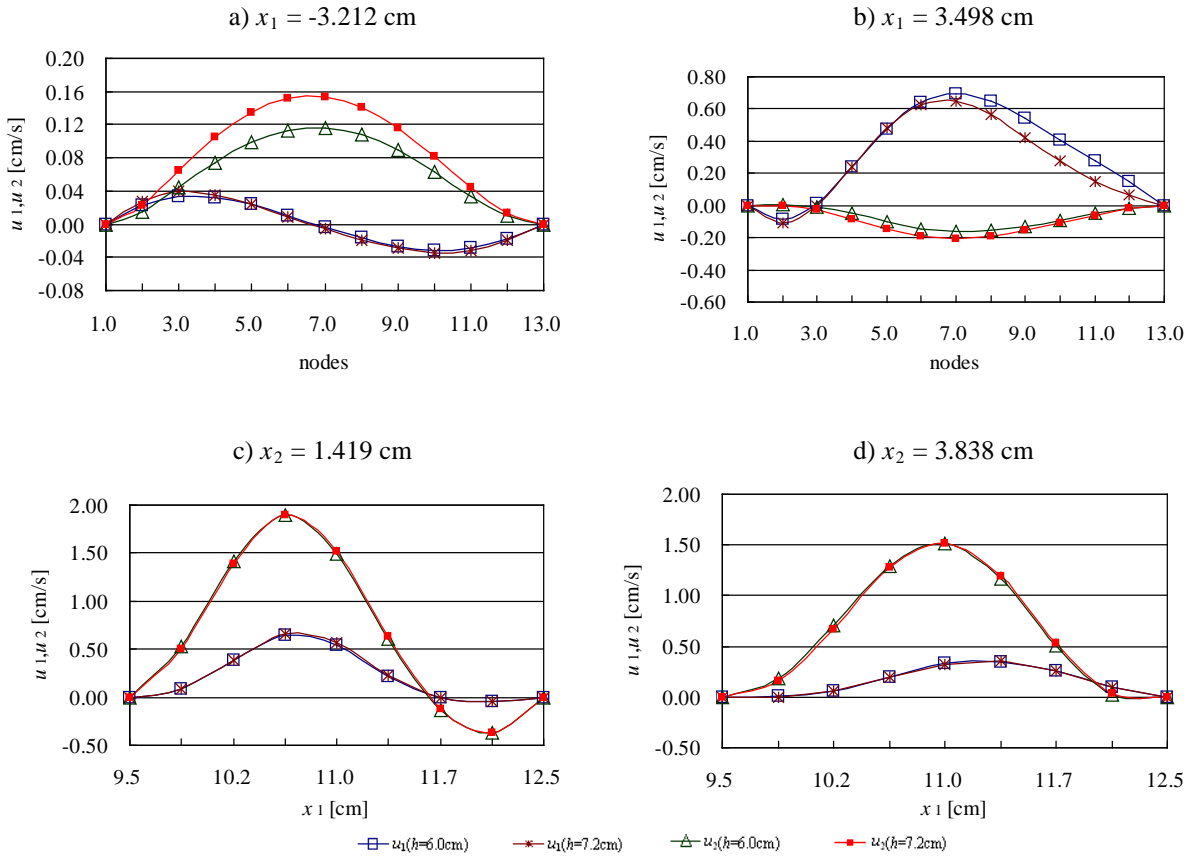


Fig. 11: Velocity profiles with chamber height 6.0 cm and 7.2 cm for valve opening 1.125 cm

Table 1: Values of velocity and jet angle at metering port for different conditions

	x_1 [cm]	x_2 [cm]	u_1 [cm/s]	u_2 [cm/s]	$\tan\alpha$	α	$u = \sqrt{u_1^2 + u_2^2}$ [cm/s]
$x_v = 0.375$ cm	9.867	0.473	1.4158	3.1099	2.1966	65.5226°	3.4170
$x_v = 0.750$ cm	9.867	0.000	1.3283	2.6640	2.0056	63.4989°	2.9768
$x_v = 1.125$ cm	9.867	0.000	0.9465	1.8072	1.9031	62.2799°	2.0415
Chamber height 7.2 cm ($x_v = 1.125$ cm)	9.867	0.000	0.9398	1.8018	1.9182	62.4660°	2.0320
Chamber length 9.6 cm ($x_v = 1.125$ cm)	11.375	0.000	0.9548	1.8031	1.8814	62.0081°	2.0420

Table 1 lists the values of velocity and jet angles at the metering port for different conditions. The jet velocity and the jet angle are greatest when the valve opening is 0.375 cm. With the valve opening being widened, the jet velocity and jet angle is lowered. The jet velocities and jet angles change little when altering the chamber length and chamber height. For a spool valve, the steady state flow force is determined by

$$F_{\text{flow}} = \rho q u \cos \alpha \quad (46)$$

Here ρ is the density of the fluid, $q = c_d \pi D x_v \sqrt{2\Delta p / \rho}$ is the flow rate passing through the valve, c_d is the flow discharge coefficient, D is the spool diameter, Δp is the pressure difference across the metering port, $u = c_v \sqrt{2\Delta p / \rho}$ is the velocity, c_v is the velocity coefficient and α is the jet angle. Since ρ , q ,

and inlet pressure p have been kept constant in the numerical simulation, the steady state flow force is determined by velocity u and jet angle α . When x_v is 0.375 cm, F_{flow} is $1.4158\rho q$. When x_v is 0.75 cm and 1.125 cm, F_{flow} is $1.3283\rho q$ and $0.9496\rho q$, respectively. This means that the steady state flow force decreases when the valve opening is enlarged. The jet velocity is higher when the valve opening is smaller, this indicates that the pressure drop across the metering port is higher, and more restriction is exerted on the fluid than in the case of a larger valve opening. This means that much energy loss is produced at the metering port when the valve opening is smaller.

4 PIV Experiments

4.1 Principle of Particle Image Velocimetry (PIV)

The particle image velocimetry (PIV) technique is a powerful whole-field velocity measuring tool. PIV differs from Laser Doppler Anemometry (LDA) in that it can measure the whole velocity field simultaneously, and LDA can only obtain a local velocity at a time. PIV removes the drawback of hot-wire and hot-film anemometers in that it does not disturb the flow. The principle of PIV is to measure the distance Δs of tracing particles moving with the fluid during a very short known time interval Δt , then the velocity u is calculated by (Adrian, 1991)

$$u = \frac{\Delta s}{\Delta t} \quad (47)$$

The flow medium is seeded with particles that are assumed to follow the flow, and the velocity of the particle is equal to the velocity of the fluid. Laser light is modulated with concave and convex lenses into a thin light sheet to illuminate the test section with seeding particles twice in a very short time interval. A fast frame-transfer CCD camera is utilized to record two images exposed by laser pulses. The images captured are then processed by FFT cross-correlation algorithm to obtain the information of velocity and other physical quantities. The results can be displayed in the form of velocity vector plots or contours.

4.2 Facility used for PIV Experiments

There is a fluid circulation system for PIV experiments. The system consists of a reservoir for containing fluid with tracing particles, a pump-motor component for providing energy to the circulating fluid, two rotating flowmeters with different measuring ranges for indicating the flow rate passing through the test model, the spool model being tested, pipes for connecting the components, and valves for controlling the flow rate and flow direction.

In the PIV experimental system, the illumination source is two pulsed Nd: YAG lasers. The temporally separated green laser pulses are aligned so the beams are spatially overlapped. The energy of each laser is 200 mJ, laser wavelength is 532 nm, pulse width is 4-6 ns. One convex and one concave lens are used to form a 1.5-2.0 mm thickness light sheet, and a mirror is arranged to reflect the laser sheet on the test section. Polystyrene spherical particles with a diameter of 30-50 μm are seeded into the fluid as a tracing particle. The camera that captures the images is Kodak Mageplus ES1.0 CCD arrays. Its frame rate is 15 Hz for cross-correlation with a resolution of 1008 \times 1018 pixels. The frame grabber board is an EPIX image card with a 68 pin SCSI interface. The computer is DELL PII 450 with 256MB RAM. The FFT cross-correlation algorithm is used in image processing software. The results of PIV experiments are post processed and visualized in the form of a velocity vector plot.

4.3 PIV Results

The PIV test model is shown in Fig. 12. It is made of a transparent acrylic sheet with a thickness of 4 mm, and its opening is 3.75 mm, its width (normal to the side walls) is 7 cm.

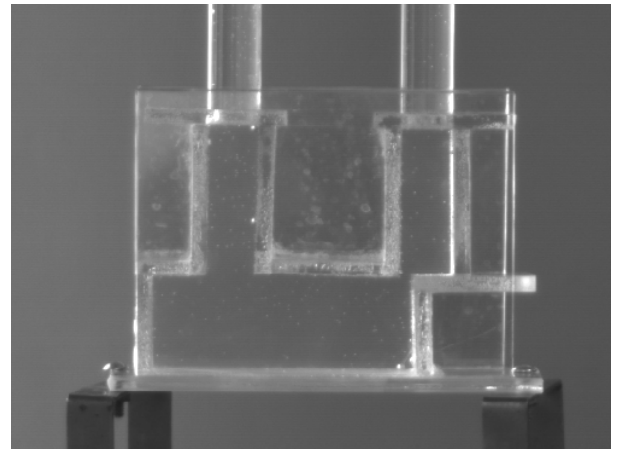


Fig. 12: Test model of the spool valve

Particle images with time intervals of 1.5 ms are recorded. The flow direction is from left to right. For the convenience of comparing the results of PIV with that of FEM, a 49 \times 32 mesh structure is used to process the particle images. The flow domain of both PIV experiments and the FEM simulation has a total of 895 nodes. Figure 13 a) shows the processing results of PIV in the form of velocity vectors plot. Figure 13 b) demonstrates the results of FEM simulation. In Fig. 13 a), a large vortex is observed on the lower left zone of the valve chamber. The size of the vortex by PIV is bigger than that shown in Fig. 13 b) by FEM calculation. The center of the vortex by PIV is located at about (-2.2, -2.5), while by FEM the center is about (-2.0, -2.9). In the center of the chamber, the flow direction is not regular; it is up and down from time to time, and there exists a small vortex near the metering port that is different from the numerical simulation in position, size, and intensity. The difference comes from the three-dimensional effects of the test model. The fluid not only flows in the plane determined by x_1 and x_2 , but also flows from front to back. In the outlet passage, the flow structure seems not so reasonable, and it is different from that of the FEM simulation. It is easy to see from the particle images that there are two dark strips on the outlet passage, and the tracing particles could not be seen clearly. The reason is that the laser sheet accesses from the bottom of the model, and the lower right vertical wall blocks the laser sheet.

Figure 14 shows the horizontal velocity vector profiles by PIV and FEM at four different x_1 positions. Figure 14 a) and b) are the results of the lower left area of the valve chamber for $x_1 = -3.212$ cm and $x_1 = -2.784$ cm. The velocity value by PIV is higher than that by FEM simulation near the up wall of the chamber. The velocity matches well in the middle parts. Near the bottom wall of the chamber, the value of negative velocity by PIV is larger than that by FEM. Figure 14 c) and d) are the results of the central region of the valve chamber for $x_1 = 3.5$ cm and $x_1 = 4.164$ cm. The

velocities do not match. The velocity value by PIV is very small: the maximum velocity is less than 0.1 cm/s, while by FEM it is nearly 0.62 cm/s.

Figure 15 shows the vertical velocity vector profiles by PIV and FEM at four different x_1 positions. Figure 15 a) and b) are the results at the region of the lower left side of the valve chamber for $x_1 = -3.212$ cm and $x_1 = -2.784$ cm. The velocity profile matches well except that near the up wall of the chamber, the velocity by PIV is higher than that by FEM for $x_1 = -3.212$ cm. For $x_1 = -2.784$ cm, the maximum velocity value by FEM is 0.15 cm/s, while by PIV it is only 0.06 cm/s. Figure 15 c) and d) are the results of central parts of the valve chamber for $x_1 = 3.5$ cm and $x_1 = 4.164$ cm. PIV and FEM have the same velocity distribution trend, but have different value, and different peak velocity points. For $x_1 = 3.5$ cm, the maximum value of negative velocity by PIV is nearly 0.09 cm/s at the point of $x_2 = -4.5$ cm, while by FEM the maximum value of negative velocity is 0.12 cm/s at the point of $x_2 = -3.0$ cm. For $x_1 = 4.164$ cm, the maximum values of positive velocities by PIV and FEM are 0.016 cm/s and 0.032 cm/s, respectively at the point of $x_2 = -1.5$ cm. The peak negative velocities by PIV and FEM are -0.11 cm/s and -0.032 cm/s at the points of $x_2 = -4.5$ cm and $x_2 = -3.75$ cm respectively.

To get clearer particle images of the outlet passage, the laser sheet accessing direction is changed: it is from right to left. Particle images of the outlet passage with a time interval of 1.5 ms are captured. The corresponding velocity vector plot is displayed in Fig. 16 a). Figure 16 b) is the velocity vector plot of the outlet passage by FEM. For comparison purposes, both Fig. 16 a) and Fig. 16 b) use the same mesh structure of 9×20 , and a total of 180 nodes are used. In Fig. 16 a), there exists a vortex that is a little different from that in Fig. 16 b) by

FEM simulation. The vortex size by PIV is larger than that by FEM, but its intensity is weaker than that by FEM. The vortex center by PIV is about in the location of (11.75, 2.5), while by FEM the vortex center is about in the position of (11.5, 2.2). That means the vortex center by PIV and FEM is almost the same. Figure 17 shows the horizontal and vertical velocity profiles by FEM and PIV at two x_2 positions, respectively. Figure 17 a) and b) are the horizontal velocity profiles for $x_2 = 1.419$ cm and $x_2 = 1.892$ cm. PIV results show a very small negative horizontal velocity; it is not reasonable. Figure 17 c) and d) are the vertical velocity profiles for $x_2 = 1.419$ cm and $x_2 = 1.892$ cm. They have the same velocity distribution trend, but the velocity magnitude and peak velocity points are little different. The differences are from the effects of three-dimensional flow of the fluid within the test model. There are also some other factors that can bring errors to the PIV results, such as the inaccuracy in making the test model, the effectiveness of the image processing algorithm, etc.

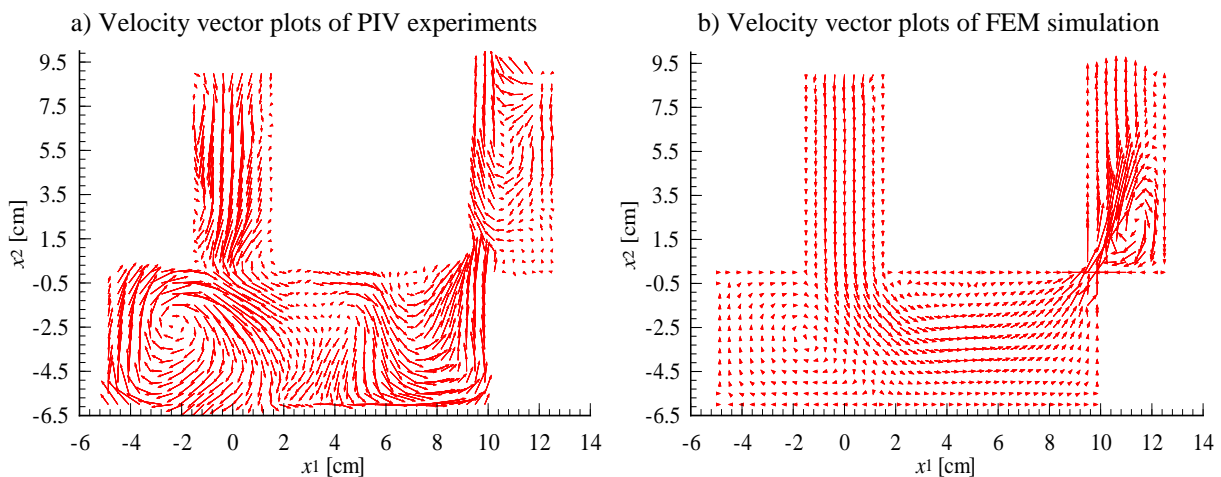


Fig. 13: Velocity vector plot of the whole spool valve with PIV experiments and FEM simulation

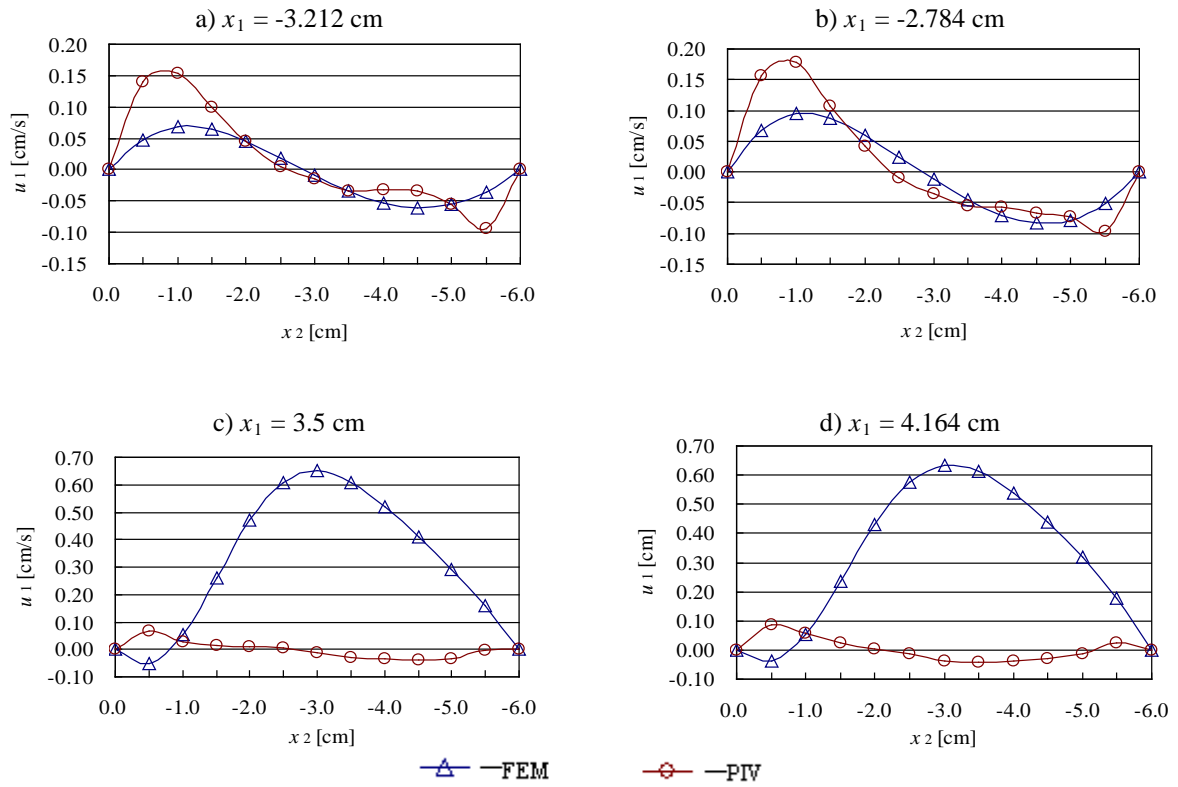


Fig. 14: Comparison of horizontal velocity profiles of FEM and PIV for different x_1 positions

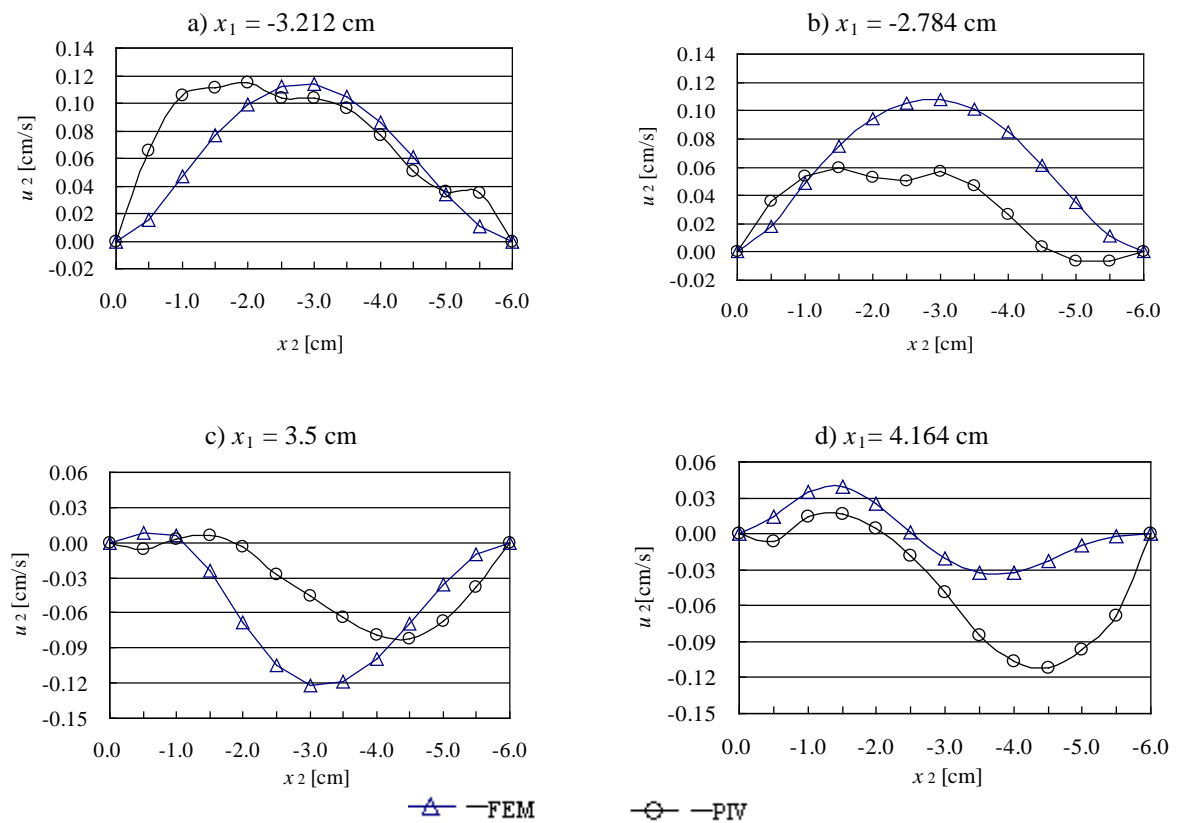


Fig. 15: Comparison of vertical velocity profiles of FEM and PIV for different x_1 positions

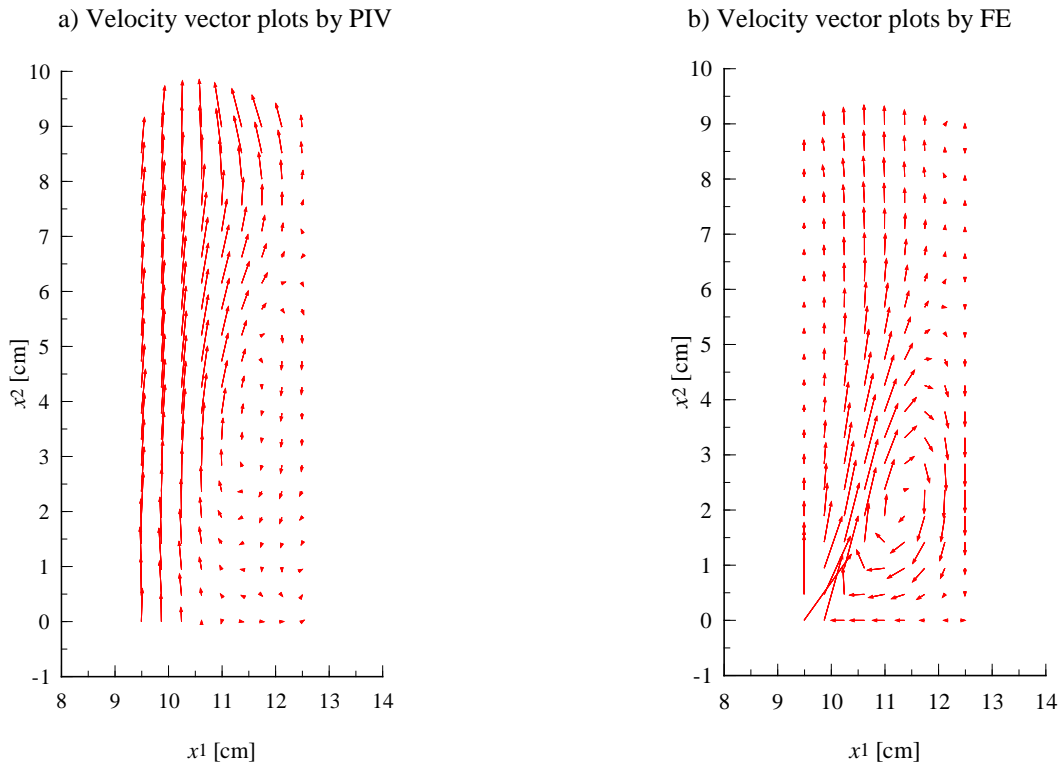


Fig. 16: Velocity vector plots of outlet passage with PIV and FEM methods

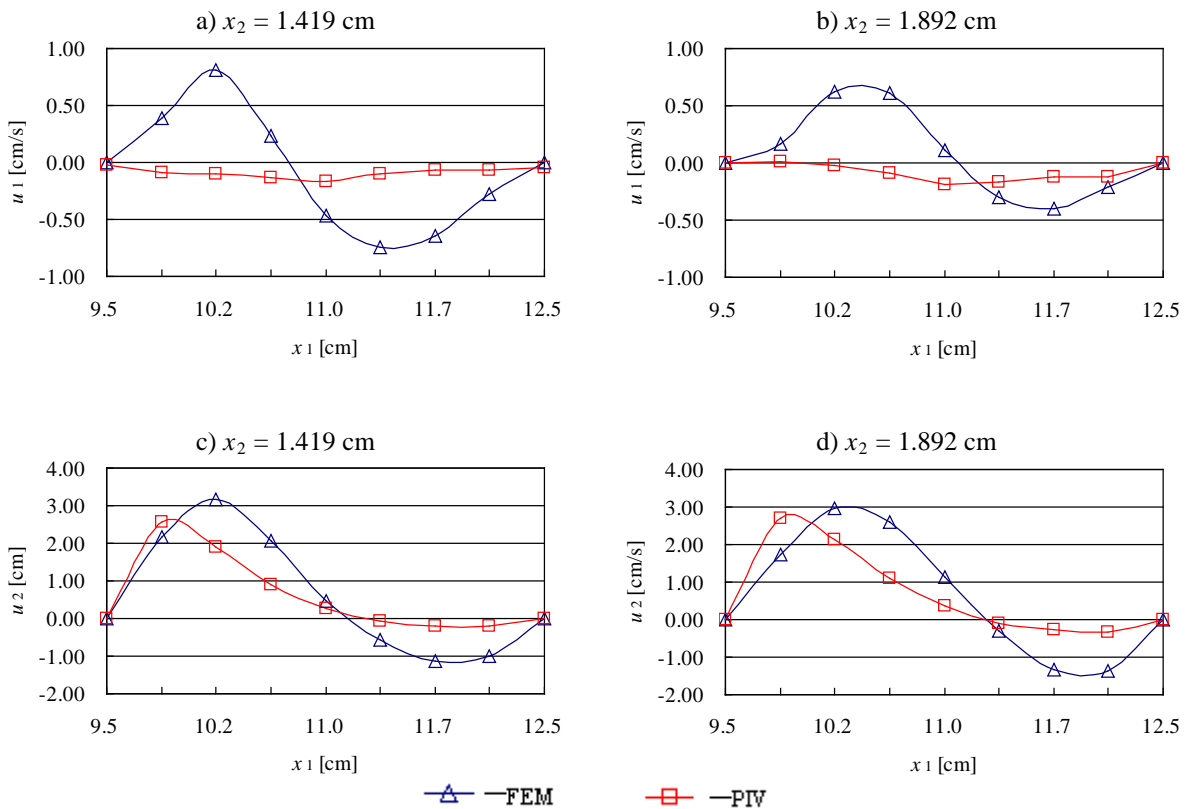


Fig. 17: Comparison of horizontal and vertical velocity profiles of FEM and PIV for different x_2 positions

5 Conclusion

(i) For metering-out spool valves, FEM numerical simulation and PIV experiments have shown that the flow structure is complex. There are three main vortices formed inside the valve, the one with the biggest size is on the lower left side of the chamber, the second one with the smallest size is on the upper center of the chamber, and the third one with the greatest intensity is on the upper right corner of the outlet passage near the metering port.

(ii) When the valve opening is varied, the size and the intensity of the three vortices vary accordingly. With the increase of the valve opening, the intensity of the vortex on the lower left side of the chamber increases and its size changes a little. The upper center vortex remains almost unchanged, and the one near the metering port decreases in size and intensity.

(iii) When changing the valve chamber height or chamber length, the flow structure changes only a little at the upper left side of the outlet passage near the metering port, where another very smaller vortex is formed. This means that changing the valve chamber has no strong effect on the flow structure.

(iv) When keeping the inlet flow rate and pressure constant, the steady state flow force decreases when the valve opening is enlarged. The jet velocity is higher when the valve opening is smaller. This means that the pressure difference across the metering port is higher, and more restriction is exerted onto the fluid than in the case of larger valve openings.

(v) The main flow structure found from the FEM simulation and PIV experiments is almost the same, though there is a little difference in some regions. The difference is that FEM simulation uses the ideal two-dimensional mathematical model, and the PIV experiment test model is three-dimensional in fact.

(vi) The particle image velocimetry technique is a powerful whole-field velocity measuring tool, which is very useful for validating the numerical simulation. But the accuracy of PIV results is affected by many factors, such as the fabricating technique of the test model, laser sheet quality, the feature of the tracing particle, and the image processing algorithm, et al. Much attention should be given to these factors in PIV experiments.

Nomenclature

$\mathbf{A}_{ij}^{(e)}$	coefficient matrix of local equation	[-]
\mathbf{A}_{nm}	coefficient matrix of global equation	[-]
$\mathbf{B}_{ijk}^{(e)}$	coefficient matrix of local equation	[-]
\mathbf{B}_{nmp}	coefficient matrix of global equation	[-]
c_d	flow discharge coefficient	[-]
$\mathbf{C}_{ij}^{(e)}$	coefficient matrix of local equation	[-]
\mathbf{C}_{nm}	coefficient matrix of global equation	[-]
c_v	velocity coefficient	[-]
D	spool diameter	[-]

$\mathbf{D}_i^{(e)}$	coefficient vector of local equation	[-]
\mathbf{D}_n	coefficient matrix of global equation	[-]
f_i	body force	[m/s ²]
$\mathbf{E}_{ij}^{(e)}$	coefficient matrix of local equation	[-]
\mathbf{E}_{nm}	coefficient matrix of global equation	[-]
F_{flow}	steady state flow force	[N]
$\mathbf{F}_{ij}^{(e)}$	coefficient matrix of local equation	[-]
\mathbf{F}_{nm}	coefficient matrix of global equation	[-]
g	vorticity boundary value	[1/s]
$\mathbf{G}_i^{(e)}$	coefficient matrix of local equation	[-]
\mathbf{G}_n	coefficient vector of global equation	[-]
i	node number of the element	[-]
\mathbf{J}	Jacobian	[-]
j	node number of the element	[-]
k	node number of the element	[-]
L	characteristic length	[m]
n	number of whole nodes	[-]
m	number of whole nodes	[-]
N_i	interpolation function of stream function	[-]
M_i	interpolation function of vorticity	[-]
p	number of whole nodes	[-]
P	kinematic pressure	[m ² /s ²]
Q	flow rate	[m ³ /s]
Re	Reynolds number	[-]
t	time	[s]
u	value of velocity of a node	[m/s]
u_i	velocity components	[m/s]
u_0	free stream velocity	[m/s]
u_s	velocity boundary value	[m/s]
x_i	Cartesian coordinate system	[m]
α	jet angle	[⁰]
ε_{ij}	permutation symbol	[-]
ψ	stream function	[m ² /s]
Ψ_m	value of stream function on global nodes	[m ² /s]
ν	kinematic viscosity	[m ² /s]
ρ	fluid density	[kg/m ³]
Γ_u	velocity boundary	[-]
Γ_ω	vorticity boundary	[-]
Δp	pressure drop across metering port	[N/m ²]
Δs	distance of particle movement in certain time interval	[m]
Δt	time interval	[s]
ω	vorticity	[1/s]
ω_i	nodal value of vorticity of local element	[1/s]
$\dot{\omega}_i$	derivative of vorticity to time on the node of local element	[1/s ²]
ω_m	value of vorticity on global nodes	[1/s]
$\dot{\omega}_m$	derivative of vorticity to time on global nodes	[1/s ²]
Ω	flow domain	[-]
η	Natural coordinate system	[-]
ξ	Natural coordinate system	[-]

Acknowledgement

The author would like to acknowledge Prof. Gongxin Shen and his PhD candidates, Runjie Wei and Zhan Huang, for their support and help in doing PIV experiments in their laboratory of fluid mechanic institute of Beijing University of Aeronautic and Astronautic.

References

- Adrian, R.** 1991. Particle-image Velocimetry for Experimental Fluid Mechanics. *Ann. Rev. Fluid Mech*, Vol. 123, pp. 261-304.
- Baker, A. J.** 1975. Finite Element Solution Algorithm for Incompressible Fluid Dynamics, *Finite Element in Fluids*. Vol. 2, Ed. Gallagher, R. H. et al, New York, John Wiley and Sons Inc., pp. 67-82.
- Baker, A. J.** 1983. *Finite Element Computational Fluid Mechanics*. New York, McGraw-Hill Book Company.
- Baker, A. J.** 1991. *Finite Elements*, 1-2-3. New York, McGraw-Hill, Inc.
- Bao M., Fu, X. and Chen, Y.** 2001. Computational Fluid Dynamic Approach to Pressure Loss Analysis of Hydraulic Spool Valve. *Proceedings of the 5th International Conference of Fluid Power Transmission and Control*, Hangzhou, China.
- Borghi, M., Milani, M. and Paoluzzi, R.** 2000. Stationary Axial Flow Forces Analysis on Compensated Spool Valves. *International Journal of Fluid Power*, Vol.1, No.1 pp.13-22.
- Chung, T. J.** 1978. *Finite Element Method in Fluid Dynamics*. New York, McGraw-Hill, Inc.
- Kipping, M. and Stoffel, B.** 1996. Experimental and Numerical Investigations of the Flow in Oil-hydraulic Spool Valves. *Proceedings of International Symposium on Fluid Machinery and Fluid Engineering*, Beijing, China.
- Vaughan, N. D., Jonn, D. N., and Burnell, L. R.** 1992. The Use of Computational Dynamics in Hydraulic Valve Design. *Design, Circuit, Component and System Design*, New York, John Wiley and Sons Inc. pp. 226-244.
- Wang, L., Chen, Y., Ruan, X. and Lu, Y.** 1997. Experimental Study on Fluid Flow in Fluid Power System. *The 4th International Conference of Fluid Power Transmission and Control*, Hangzhou, China.
- Wendt, J. F.** 1996. *Computational Fluid Dynamics, An Introduction*, 2nd edition. Berlin Heidelberg, Springer-Verlag.
- Ruan, X. D., Song, X. Q., Yamamoto, F., Wang, L. X. and Shao, X.** 1997. PIV Experiment of Flow Field in Spool Valve Chamber. *The 4th International Conference of Fluid Power Transmission and Control*, Hangzhou, China.
- Yuan, Q. and Li, P. Y.** 2002. Using Viscosity to Improve Spool Agility. *The 2002 Bath Workshop on Power Transmission and Control (PTMC)*, University of Bath, UK.
- Yuan, Q. and Li, P. Y.** 2002. An Experimental Study on the Use of Unstable Electrohydraulic Valves for Control. *Proceedings of the 2001 American Control Conference*, Anchorage, Alaska, USA.



Dianrong Gao

Born in 1962. Prof. Dr. of Mechatronic Department, Mechanical Engineering college, Yanshan University, P. R. China. Research interests include design and analysis of fluid power transmission and control systems, computational fluid dynamic in hydraulic components and complex flow channels, digital particle image velocimetry (DPIV), and stereoscopic particle image velocimetry (SPIV) in hydraulic valves, micro-fluidics. As a visiting scholar from Jan. 10th, 2003 to Jan. 10th, 2004 at the Department of Mechanical Engineering of Louisiana State University, USA.